

1
2 **Size Dependent Uncatalyzed Sulfite Oxidation in Aqueous Microdroplets**
3

4
5 Kedong Gong,¹ Sandhya Sethuraman,² Zifeng Tang,² V. Faye McNeill^{2,3*} and Vicki H. Grassian^{1*}
6

7 ¹Department of Chemistry and Biochemistry, University of California San Diego, La Jolla,
8 CA 92093, United States

9 ²Department of Chemical Engineering, Columbia University
10 New York, NY 10027, United States

11 ²Department of Earth and Environmental Sciences, Columbia University
12 New York, NY 10027, United States

13
14 *Corresponding Authors. Email: vhgrassian@ucsd.edu (V.H.G) and vfm2103@columbia.edu
15 (V.F.M.)
16
17

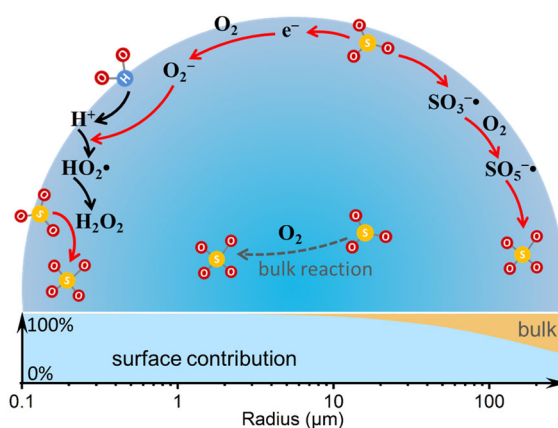
ABSTRACT

Aqueous aerosols and microdroplets exhibit unique chemical kinetics relative to the bulk phase. Aqueous aerosol and microdroplet chemistry, as it relates to multiphase atmospheric chemistry, also has major impacts on air quality and climate. Here, we have investigated uncatalyzed oxidation of sulfite (SO_3^{2-}) to sulfate (SO_4^{2-}) by O_2 in aqueous microdroplets deposited on a superhydrophobic substrate, as a function of size, gas-phase composition, and temperature utilizing an environmental cell and *in-situ* micro-Raman spectroscopy. We show that the uncatalyzed sulfite oxidation driven by O_2 in aqueous microdroplets is size-dependent across varying O_2 concentrations and temperatures. Sulfite oxidation rates scale with the surface-area to volume ratio (i.e. $1/\text{radius}$) of the microdroplet and oxidation occurs in the absence of any added catalysts. We use a resistor-based approach to model multiphase mass transfer and reaction in the experimental system and confirm that the observed size-dependent kinetics are consistent with slow bulk kinetics coupled with an efficient reaction at the interface ($k_{\text{II}} = 9.44 \times 10^{-3} \text{ M}^{-1} \text{ s}^{-1}$, $\gamma_{\text{s},0} = 9.27 \times 10^{-10}$ at 298 K and 21% O_2). Above a critical droplet radius, bulk kinetics dominate, but for sufficiently small sizes, which are relevant in the atmosphere, rates are accelerated due to the role of interfacial reaction. These results provide insights into chemistry in microcompartments and provide an outlook for improved representations of sulfate formation in atmospheric droplets and aerosols in large-scale atmospheric chemistry models.

KEYWORDS: Sulfate formation, uncatalyzed oxidation, aqueous aerosol, microcompartments, multiphase chemistry

SYNOPSIS: Efficient interfacial reactions, combined with slower bulk-phase kinetics, drive size-dependent sulfite oxidation, elucidating the mechanisms behind sulfate formation in aqueous aerosols.

TOC:



1. INTRODUCTION

Aqueous microdroplets are unique microreactors; compared to bulk phase solutions, the air-water interface in these systems enhances reaction rates and enables redox chemistry.¹⁻¹⁰ This has been ascribed to enhanced mass transfer,¹¹ differences in bulk and surface pH,¹² molecular orientation, interfacial propensity, and interfacial electric field effects.¹³⁻¹⁵ Interfacial electric field effects have been suggested to contribute to redox processes.¹⁵⁻¹⁸ Examples include the spontaneous oxidation of salicylic acid and aromatic sulfones,¹⁹⁻²⁰ changes in oxidation states of interfacial iodine,²¹ and the spontaneous generation of hydrogen peroxide (H₂O₂).^{8, 22-23} However, the dominant factors for interfacial enhancement of specific reaction pathways continue to be poorly understood, inhibiting our ability to model these important processes in an atmospheric chemistry context.

The oxidation of S(IV) (SO₃²⁻, HSO₃⁻, and/or SO₂·H₂O) to form S(VI) (SO₄²⁻, HSO₄⁻, and/or H₂SO₄) is fundamental for understanding air quality (haze formation) and acid rain. However, urban haze events in Asia are inadequately explained by current mechanisms including only cloudwater processes derived from bulk phase aqueous chemistry, which successfully model sulfate formation in the U.S. and Europe.²⁴ The missing sulfate content scales with the aerosol water content,²⁵ indicating that the multiphase oxidation of SO₂ in or on aqueous aerosols plays a critical role in more polluted environments. Since S(IV) oxidation pathways are highly sensitive to ionic strength and the pH of the reaction medium, as well as the role of the gas-aerosol interface, it is not possible to directly extrapolate the reaction mechanisms and kinetics for cloud-water conditions to aerosol conditions, necessitating laboratory and modeling studies in the aqueous aerosol.²⁶⁻³⁰

Recent studies suggest that S(IV) oxidation is accelerated in micron-sized aqueous aerosols compared to bulk solutions^{3-5, 26-35} This includes different microdroplet-mediated S(IV) oxidation pathways such as uncatalyzed oxidation,²⁶⁻²⁸ transition metal ion (TMI)-catalyzed interfacial oxidation,⁴⁻⁵ and interfacial NO₂-assisted oxidation.^{3, 36} Several mechanisms have been proposed for these reactions. Zhong et al.³³ suggested that an H₂O···SO₂ intermediate at the interface contributes to the solvation of SO₂ at the water surface. The Hoffmann group observed rapid S(VI) formation via the uncatalyzed oxidation pathway by a direct interfacial electron transfer from S(IV) to O₂ to form sulfur radical species at the droplet surface.²⁷⁻²⁸ Both the reduced hydrogen-bonding network of water molecules at the gas-aqueous interface and interfacial electric fields play a significant role in the oxidation reaction.^{3, 20, 23, 36-37}

Uncatalyzed oxidation, wherein S(IV) is oxidized directly by O₂,³⁸ has been relatively less studied, in part because the first-order rate constant (~10⁻⁵ s⁻¹) in bulk solution is too slow to be atmospherically significant, particularly at atmospherically relevant pH.^{35, 39} However, recently, Hung et al.²⁷ demonstrated that the rate of this uncatalyzed oxidation is approximately 1-2 orders of magnitude higher than that by H₂O₂ oxidation for 1.0 ppbv H₂O₂ interacting with 50 µg/m³ of aerosols with diameters of 1-16 µm. Chen et al.²⁶ showed that the SO₂ uncatalyzed oxidation in the aqueous droplets with radii of 4-7 µm is much faster than TMI-catalyzed oxidation at high ionic strength and acidic conditions (pH 3.5-4.5). Additionally, Li et al.³⁵ reported that S(IV) oxidation through different oxidation pathways, including uncatalyzed oxidation, scales with droplet surface area, highlighting the significant influence of droplet size on this reaction. Given the rapid oxidation

rate in aqueous droplets, the uncatalyzed reaction may significantly contribute to atmospheric sulfate formation. However, until now there has been insufficient experimental data and no modeling framework to enable representation of this process in atmospheric chemistry models in order to test its environmental significance.⁴⁰⁻⁴¹

In this study, we measured the oxidation of SO_3^{2-} in microdroplets deposited on a superhydrophobic substrate using micro-Raman spectroscopy to better understand dissolved sulfite oxidation as a function of microdroplet size, gas-phase oxygen concentration, and temperature. We used an additive resistance-based model to analytically simulate multiphase mass transfer and reactions, showing that the observed size-dependent kinetics are consistent with an efficient interfacial reaction coupled with slower bulk kinetics.

2. METHODS

2.1 Chemicals and Materials

Sodium sulfite (98.5%) was purchased from Thermo Scientific. Sodium sulfate ($\geq 99.0\%$, certified ACS), sodium chloride ($\geq 99.0\%$, certified ACS), and hydrochloric acid solution (1 M) were obtained from Fisher Chemical. The quartz substrates for supporting the microdroplet were purchased from Alfa Chemistry. The Cab-O-SIL[®] TS-720 was purchased from Innoxia Ltd. All gases, including nitrogen (medical national formulary grade), oxygen (ultra-high purity grade), and a mixture containing 21% oxygen balanced in nitrogen, were sourced from Airgas. Milli-Q water ($18.2 \text{ M}\Omega \cdot \text{cm}^{-1}$, 4 ppb of Total-Organic-Carbon (TOC)) used for all experiments was obtained from a Milli-Q[®] Advantage A10[®] Water Purification System (Millipore SAS - Molsheim, France). The superhydrophobic substrate, with a contact angle of $160.1 \pm 3.35^\circ$ (see Figure S1), was produced by dip-coating a quartz plate into a solution of Cab-O-SIL[®] TS-720 suspended in acetone (20 mg/ml), followed by air drying at 200 °C on a hot plate.⁴²

2.2 Micro-Raman Spectroscopy Experiments

Bulk solutions were prepared with oxygen-free Milli-Q water (Milli-Q water purged with nitrogen) in order to reduce the potential influence of water-soluble oxygen. The 1.2 mol/kg Na_2SO_3 solution was prepared with an initial pH of 9.5. This pH was not further adjusted because at this pH, there is essentially one S(IV) species, SO_3^{2-} , presented in the bulk solution, thus limiting the number of oxidation reactions taking place in the solution and simplifying kinetic analysis (Figure S2). A high pH also reduces the potential influence of trace concentrations of TMI (i.e. catalyst species) that inevitably originate from Milli-Q water or the chemical reagents used here, according to previous studies.^{4, 43} Microdroplets were generated from the bulk solutions by using a nebulizer and collected on a superhydrophobic quartz substrate. The hydrophobic substrate with aerosols was transferred to a sealed environmental cell (Linkam, THMS600 Stage) connected to a humidity control system (see Figure S3). The relative humidity (RH) within the environment cell was set at $\sim 80 \pm 3\%$. This was controlled by adjusting the ratio of dry and wet gases and monitored by a hygrometer (Buck, CR-4).⁴ The droplets were monitored *in-situ* with micro-Raman spectroscopy (Horiba, LabRam HR Evolution). The spectrometer is equipped with an optical microscope

(Olympus BX41), featuring 10× and 100× objectives, and a 532 nm laser. All spectra were collected with a 5-second acquisition time and 2 co-added accumulations.

2.3 Quantification of Sulfate and Sulfite Concentrations

To quantify the concentrations of sulfate ($[\text{SO}_4^{2-}]$) and sulfite ($[\text{SO}_3^{2-}]$) within the microdroplets during the oxidation reaction, calibration curves were established. The calibration curves of $[\text{SO}_4^{2-}]$ and $[\text{SO}_3^{2-}]$ were obtained from the peak area ratios of sulfate ($\nu_s(\text{SO}_4^{2-})$ at 980 cm^{-1}) or sulfite ($\nu_s(\text{SO}_3^{2-})$ at 934 cm^{-1} and $\nu_a(\text{SO}_3^{2-})$ at 966 cm^{-1}) respectively to water ($\nu(\text{OH})_{\text{water}}$ at 3420 cm^{-1} , a broad peak from 2700 to 3800 cm^{-1}). These peak areas were derived from the Raman spectra of standard Na_2SO_4 and Na_2SO_3 solutions at various concentrations in units of molality (m , mol/kg). The Raman peak for H_2O , $\nu(\text{OH})_{\text{water}}$, was applied as an internal standard.¹² The sulfate calibration curve was constructed first with an excellent linear correlation (see Figure S4). The sulfate concentration was determined as follows, where k_{sulfate} represents the slope of 46.7 m determined from the calibration curve.

$$[\text{SO}_4^{2-}] = k_{\text{sulfate}} \frac{A(\text{SO}_4^{2-})}{A(\text{OH}_{\text{water}})} \quad (1)$$

Interestingly, even in the fresh Na_2SO_3 solution, small amounts of SO_4^{2-} are present, showing that the Na_2SO_3 solution can be oxidized under air. Therefore, the Raman spectra of standard Na_2SO_3 solutions were collected under nitrogen to prevent further oxidation by air. As shown in Figure S5a, the Raman peak of $\nu_s(\text{SO}_3^{2-})$ is accompanied by a smaller peak of $\nu_s(\text{SO}_4^{2-})$ at 980 cm^{-1} .⁴⁴ However, this coupled peak hinders the quantification of the $\nu_s(\text{SO}_3^{2-})$ peak area. Hence, a peak analysis method was employed to determine the peak area of $\nu_s(\text{SO}_3^{2-})$ after curve fitting the $\nu_s(\text{SO}_4^{2-})$ peak (Figure S5b). Subsequently, the calibration curve of sulfite was obtained (Figure S5c). The sulfite concentration was determined based on equation 2, where k_{sulfite} is the slope of 67.1 m in Figure S5.

$$[\text{SO}_3^{2-}] = k_{\text{sulfite}} \frac{A(\text{SO}_3^{2-})}{A(\text{OH}_{\text{water}})} \quad (2)$$

2.5 Kinetic Data Analysis and Modeling

Generally, the aqueous sulfite oxidation process (reaction R1) is influenced by the concentration of oxygen and sulfite.



The oxygen concentration is roughly constant (21% of air) in the atmosphere. This uncatalyzed oxidation is considered to be a first order process with respect to sulfite.^{26, 35} Then the time evolution of sulfite concentration, $C_{\text{sulfite}, t}$, is described by:

$$-\frac{dC_{\text{sulfite}}}{dt} = \frac{1}{\tau_{\text{sulfate}}} C_{\text{sulfite}} = \frac{dC_{\text{sulfate}}}{dt} \quad (3)$$

$$\ln\left(\frac{C_{\text{sulfite}}}{C_{\text{sulfite},0}}\right) = -\frac{1}{\tau_{\text{sulfate}}} t \quad (4)$$

The values of the inverse sulfate formation timescale ($1/\tau_{\text{sulfate}}$, min^{-1}) were determined by fitting $\ln(C_{\text{sulfite},t}/C_{\text{sulfite},t=0})$ as a function of t following Equation 4 (see Figures S6 to S9 for two different O_2 concentrations and three different temperatures). $1/\tau_{\text{sulfate}}$ was analyzed as a function of these experimental parameters for different values of droplet radius, r (μm), which was measured with the optical microscope equipped on the micro-Raman spectrometer.

We further analyzed reaction kinetics in the sulfite oxidation system using an additive resistance approach following Worsnop et al.⁴⁵ In a multiphase system, many potential processes, including gas or in-particle diffusion, mass accommodation, slow or fast bulk reactions, and reactions at the surface of the particle could be taking place in series or in parallel. The relative timescales of these processes determine the overall rate of the process, as well as the characteristic shape of the measured sulfate concentration profiles and the apparent dependence on particle size, O_2 concentration, and temperature. Further details are provided in section 3.3.

3. RESULTS AND DISCUSSION

3.1 Size Dependent Kinetics

Figure 1a presents the Raman spectrum of a sulfite oxidation reaction within an aqueous microdroplet on a superhydrophobic substrate compared to a bulk solution under 21% O_2 condition and 298 K in the environmental chamber held at 80% RH. The superhydrophobic substrate keeps the geometry of microdroplets nearly spherical and the radius of the droplets was stable during the reaction (see Figure S10). The dominant species, sulfite ($\nu_s(\text{SO}_3^{2-})$ at 934 cm^{-1} and $\nu_a(\text{SO}_3^{2-})$ at 966 cm^{-1}), was observed.^{4, 46} As the reaction progresses, the Raman peak for sulfate, $\nu_s(\text{SO}_4^{2-})$ at 980 cm^{-1} increases. This oxidation rate increases as the microdroplet size decreases. Notably, for a $1.8\text{ }\mu\text{m}$ microdroplet, the $\nu_s(\text{SO}_3^{2-})$ decreases significantly within 16 minutes, accompanied by a significant increase in the $\nu_s(\text{SO}_4^{2-})$ peak intensity. This observation suggests that the microdroplet environment accelerates sulfate production.

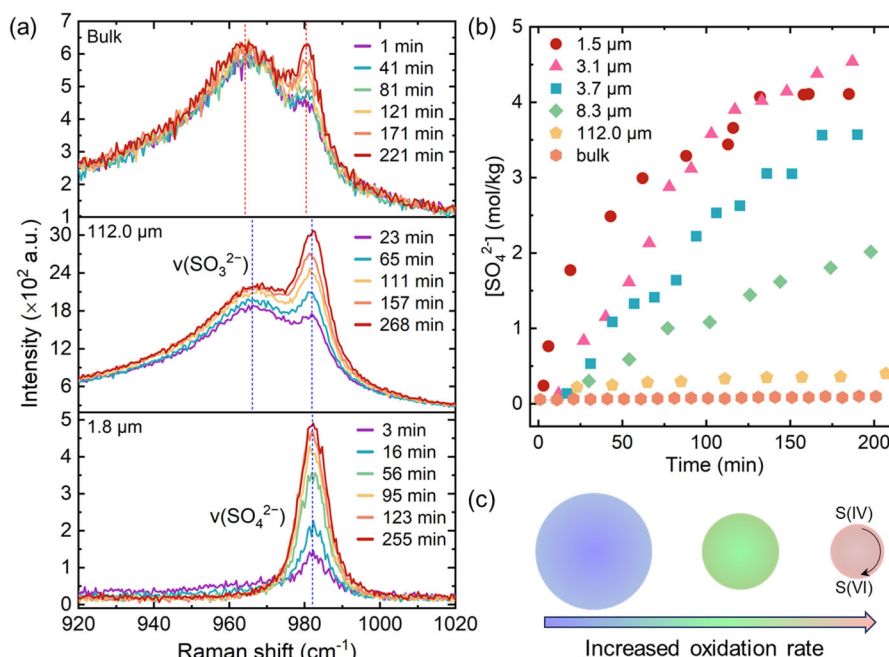


Figure 1. Sulfate formation in single microdroplet with micro-Raman spectroscopy. (a) Representative Raman spectra as a function of time for bulk solution and sodium sulfite microdroplets with radius of 112.0 and 1.8 μm under 21% O₂. (b) Time evolution of the SO₄²⁻ concentration ([SO₄²⁻]) for aqueous microdroplets of varying radius and a bulk solution based on the calibration curves of [SO₄²⁻] and [SO₃²⁻]. (c) The schematic diagram displaying the size-dependent oxidation. All spectra were collected at 298 K with RH of ~80 ± 3%.

The reaction kinetics were tracked *in-situ* for sulfite ([SO₃²⁻]) and sulfate ([SO₄²⁻]) concentration. Figure 1b shows the time evolution of [SO₄²⁻] within both bulk solution and microdroplets with radius ranging from 1.5 to 112.0 μm, indicating that the sulfate production rate increased with decreasing microdroplet radius. A continuous increase in [SO₄²⁻] was observed for bulk solution and large microdroplets (≥3.7 μm), which is in accordance with the results reported by Wang et al.⁵ and Jing et al.³¹ For the 8.3 μm microdroplet with sulfite as the sulfur source and no catalyst, an inverse sulfate formation timescale (1/τ_{sulfate}) of 2.84×10⁻³ min⁻¹ was observed, which is similar to that (2.25 ×10⁻³ min⁻¹) reported by Li, et al. for uncatalyzed oxidation of S(IV) by oxygen in the 7.0-μm microdroplet. The oxidation rate constant further increased to 2.75×10⁻² min⁻¹ when the radius of the aqueous aerosol decreased to 1.5 μm, which is more than two orders of magnitude higher compared to that in the bulk solution (1.93×10⁻⁴ min⁻¹). These results suggest an enhanced uncatalyzed oxidation in the small aqueous aerosol (Figure 1c) and highlight the significant role of the aerosol size and interface in sulfate formation.³⁵

3.2 O₂ Concentration and Temperature Dependence of Sulfate Formation

For air-water interfacial reactions, the reaction rate scales with the surface-to-volume ratio (S/V, i.e., 3/r). Figure 2a shows a linear relationship between 1/τ_{sulfate} and the inverse microdroplet radius

(r) under 9% and 21% O₂ conditions. $1/\tau_{\text{sulfate}}$ increased with decreasing microdroplet size, and rates were slower under 9% O₂. This finding is consistent with our expectations that O₂ drives oxidation in this system. This is further demonstrated in control experiments: no oxidation was observed after replacing 21% O₂ with N₂ (0% O₂), as depicted in Figure 2a. These results demonstrate that this uncatalyzed oxidation occurs at the air-water interface for droplets deposited on a superhydrophobic surface.

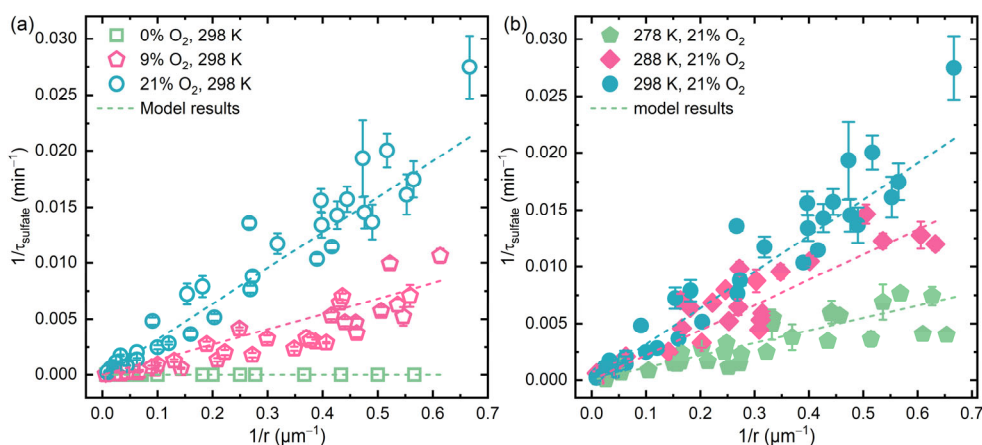


Figure 2. Reaction kinetics of sulfite oxidation within single microdroplet under different ambient conditions. (a) The inverse sulfate formation timescale ($1/\tau_{\text{sulfate}}$) scales with the inverse of the droplet radius ($1/r$) under different oxygen concentrations (0%, 9%, and 21%). All spectra were collected at 298 K with a RH of $\sim 80 \pm 3\%$. (b) $1/\tau_{\text{sulfate}}$ scales with the inverse of the droplet radius under different environmental temperatures (278, 288, and 298 K). All spectra were collected at 21% O₂ with a RH of $\sim 80 \pm 3\%$. Dashed lines represent the model simulation results (Section 3.3).

These experiments were also carried out at three different temperatures (298, 288, and 278K) to study the effect of temperature on sulfite oxidation rates. Figure 2b shows $1/\tau_{\text{sulfate}}$ as a function of $1/r$ at 278, 288 and 298 K. As seen, the sulfite oxidation rate increased with increasing temperature at a fixed RH of 80%. Although there is a fair amount of scatter in these single microdroplet measurements, these data show that the increasing the temperature from 278K to 298K increases the rate of sulfate formation by at most a factor of two in this size range.

3.3 Kinetic Modeling

We applied the additive resistance model to evaluate the relative contributions of possible processes in this multiphase kinetic system to the observed S(IV) oxidation. After analyzing the possible limiting cases,⁴⁵ we can eliminate some scenarios (e.g. domination by slow particle-phase reaction) based on the observed size dependence, and others based on the anticipated rate compared to our observed rates (i.e., processes limited by the rate of collision of O₂ with the surface are ruled out due to very high O₂ collision rates and moderate observed reaction rates). Additionally, we eliminate scenarios limited by in-particle diffusion or gas phase diffusion, which both have short sulfate formation timescales that are incompatible with moderate observed reaction rates, and differ

from the observed size dependence (Figure 3). We conclude that an efficient (but not fast) interfacial reaction in parallel with a slow bulk reaction best describes the experimental system. This is consistent with recent studies of S(IV) oxidation chemistry.³⁵

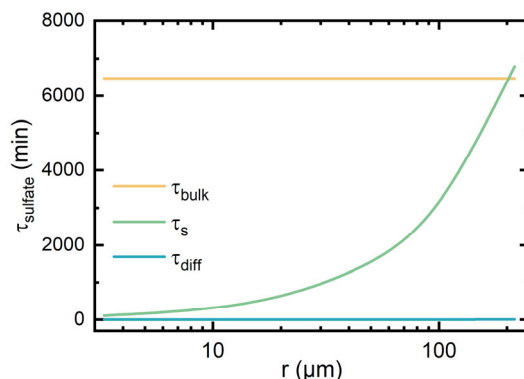


Figure 3. Timescale analysis shows that in-particle diffusion yields high rates which are unlikely to account for the moderate oxidation observed in experiments. The lines for gas phase diffusion and in particle diffusion overlap, although gas phase diffusion is even faster (timescale $\sim 10^{-7}$). The critical radius is given by the point where the timescales for the bulk-limited and surface-limited processes cross.

For this scenario, the overall uptake coefficient is represented by the resistances of the surface reaction and bulk reaction in series:⁴⁵

$$\frac{1}{\gamma_{\text{overall}}} = \frac{1}{\gamma_s + \gamma_{\text{rxn}}} \quad (5)$$

The concentration of S(IV) is given by Equation 6. The two parallel processes are encompassed in the timescale of sulfate formation, which accounts for a slow bulk reaction, in which case $[\text{O}_2]$ is uniform throughout the aerosol and is in equilibrium with the gas surrounding the particle, and an efficient interfacial reaction, where the unknown surface analogs of the Henry's law constant, rate constant, and equilibrium constant for the partitioning of SO_3^{2-} to the surface are represented by a single parameter, β (Equations 7-10).

$$[S(\text{IV})](t) = [S(\text{IV})]_0 e^{\frac{-1}{\tau_{\text{sulfate}}} t} \quad (6)$$

$$\frac{1}{\tau_{\text{sulfate}}} = \frac{-3RTn_{x(g)}\beta}{a} - HRTn_{x(g)}k_2 \quad (7)$$

$$\beta = k_{2,s}H_sK_s \quad (8)$$

$$\gamma_{s,0} = \frac{4\beta RT[S(\text{IV})]_0}{\omega} \quad (9)$$

$$\gamma_{\text{rxn},0} = \frac{4aHRT}{3\omega}k_2[S(\text{IV})]_0 \quad (10)$$

Here, H is the Henry's law constant, R is the universal gas constant T is the temperature in K, $n_{x(g)}$

is the concentration of the gas phase oxidant, ω is the thermal velocity, k_2 is the bulk rate constant, and $k_{2,s}$, H_s , K_s are surface analogs of the bulk rate constant, Henry's law constant, and equilibrium constant, respectively.

We use Monte Carlo (MC) analysis to find optimal values of k_2 and β and obtain fits from experimental data;⁴⁷ as we know, k_2 relates to γ_{rxn} and β relates to $\gamma_{s,0}$. After generating 10,000 random samples from a joint k_2 and β distribution, we minimize the weighted sum of squares between the derived concentration profile and the experimental data, where more importance is given to datasets with more points, which typically correspond to smaller radii. To assess the confidence for the fitted parameters and provide a range for potential values, we select the top 5% of samples with the smallest weighted sum of squares, i.e. those exhibiting the best performance. This analysis shows that the system is more sensitive to β than it is to k_2 . To further refine the parameter space given this relative insensitivity to k_2 , we use the critical radius reported by Li et al.³⁵ as the size where the dominant process transitions from surface to bulk kinetics (Figure 3). For uncatalyzed O₂ oxidation at pH 9, which is consistent with our experimental conditions, they reported a critical radius of 213 μm (+62/-48). We used this to place bounds on k_2 , as this radius should represent the size at which the formation timescales from the surface and bulk reactions are exactly equal. From this analysis, we determine $\beta = 8.42 \times 10^{-10}$ at 298 K, and $k_2 = 9.43 \times 10^{-3} \text{ M}^{-1} \text{ s}^{-1}$.

Using these parameters the model represents the experimental data well (Figure 2). We quantify the goodness of fit across experiments and obtain R² values ranging from 0.6 to 0.9, and with corresponding normalized RMSEs of 0.4 and 0.2 respectively (Table S1). The timescale itself depends linearly on O₂ concentration, and so the experimental observations for O₂ dependence can be readily replicated (Figure 2a). Several parameters in our system depend explicitly on temperature (including the Henry's law constant and ω), but β also exhibits temperature dependence (Equation 11). By fitting our parameters to experimental results, we derive an expression for β which applies over the given temperature range and observe the same positive correlation between high temperatures and enhanced rates as is observed in the experimental data (Figure 2b).

$$\beta = (9.15 \times 10^{-4})e^{-3.43 \frac{\text{kJ}}{\text{mol}}/RT} \quad (11)$$

We find that the overall sulfate formation timescale obtained by the model replicates experimental results for the formation timescale and concentration profile of S(VI) across temperatures (Figure 2b).

Our kinetic parameters were verified by comparing potential sulfate formation timescales to experimentally observed data for various ratios of γ_s and γ_{rxn} . We hold γ_{rxn} constant and change γ_s to be a factor of 10, 100, 1000x γ_{rxn} . Importantly, if $\gamma_s < \gamma_{rxn}$, the system would no longer exhibit the correct size dependence, making this possibility unlikely. We find that our value of γ_s , which is approximately 100x γ_{rxn} , yields timescales that are consistent with experimental results (Figure 4). We can also observe that for large particles (small 1/r), a more moderate γ_s , closer to bulk kinetics, is sufficient to match experimental data; for smaller particles (high 1/r), γ_s must be 100x γ_{rxn} to be consistent with experimental results, implying that surface chemistry is

more important in smaller particles, and significantly enhances rates. The time evolution of $[\text{SO}_4^{2-}]$ in five microdroplets with radii ranging from 1.5 to 112.0 μm was simulated using the developed model (Figure S11). The model results showed good agreement with the experimental data, further confirming the accuracy of the model.

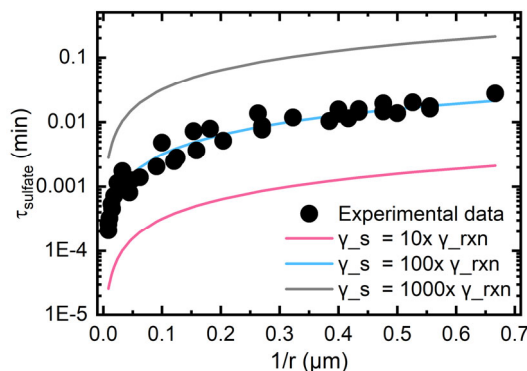
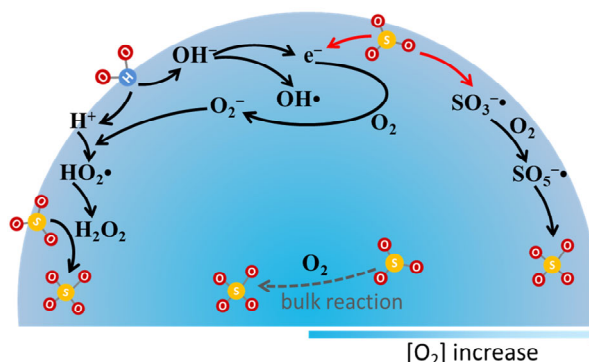
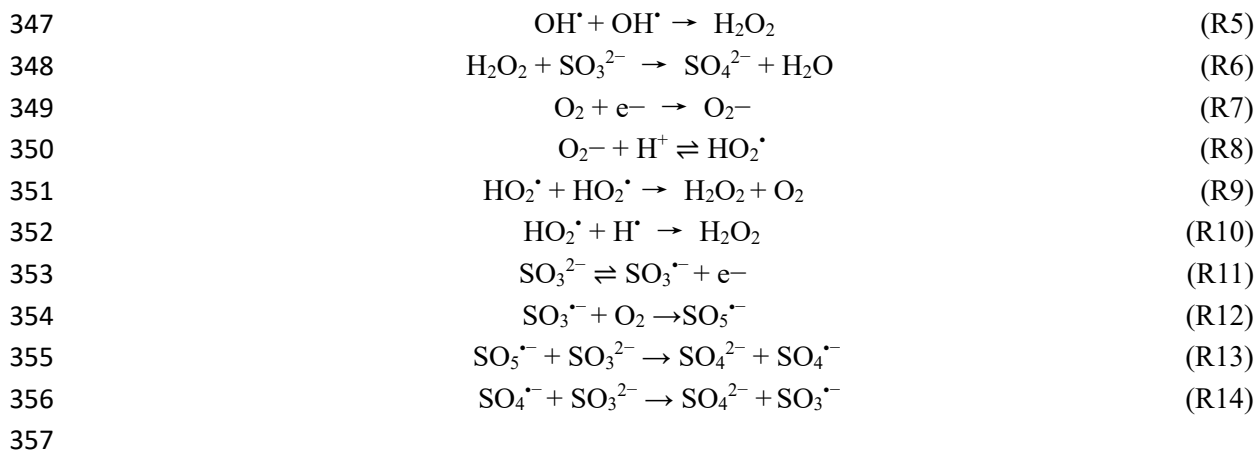


Figure 4. τ_{sulfate} vs. $1/r$ for various ratios of $\gamma_s:\gamma_{rxn}$, assuming that γ_{rxn} is held constant for a given radius, and γ_s , which is the same across all radii, changes by factors of 10. $T = 298 \text{ K}$, 21% O_2 .

3.4 Proposed Mechanism

It is well known that the hydrogen-bonding network, stratification of ions and even the self-ionization of water play roles in the unique reactions within microdroplets.^{13, 20, 23} Intriguingly, the $\nu_a(\text{SO}_3^{2-})$ and $\nu_s(\text{SO}_4^{2-})$ frequencies in the microdroplets studied here are slightly shifted from bulk values (Figure 1), which may suggest unique environments in these confined microdroplets.⁴⁸ As reported, near the air-water interface of microdroplets, water auto-ionizes to generate OH^- and H^+ ,^{23, 37, 49} producing the OH^\bullet , H atom and solvated e^- in the presence of the strong interfacial electric field (R2-R4). H_2O_2 is formed via the recombination of OH^\bullet (R5) or HO_2^\bullet (R6-R9). Furthermore, Christian and co-workers showed that OH^- facilitates H_2O_2 formation in microdroplets.⁴⁹ H_2O_2 may directly oxidize SO_3^{2-} (R6). However, in this study we observed that O_2 is required for SO_3^{2-} oxidation. This suggests either that R5 is a negligible source of H_2O_2 in this system or that R6 proceeds slowly. H_2O_2 may also be formed from O_2 via R7-R10, a mechanism which requires the participation of H^+ , although our reaction conditions are basic. It has been reported that H_3O^+ is enriched at the air-water interface while OH^- is mainly located beneath the interface.⁵⁰ OH^- also can be repelled from the interface.⁵¹ Therefore, some H^+ is available even under high pH conditions.⁴⁹ However, considering the higher charge density and greater electron-donating capability (i.e., reducing ability) of SO_3^{2-} relative to OH^- , it is also plausible to consider the formation of SO_3^\bullet and solvated e^- at the microdroplet surface (R11). SO_3^\bullet can be oxidized directly by O_2 (R12). The formed e^- can also react with O_2 at the microdroplet surface to generate O_2^\bullet (R7), thereby contributing to H_2O_2 formation.





358

359 **Scheme 1.** Schematic of proposed sulfite oxidation mechanisms at the air-water interface and

360 within aqueous aerosols.

361

362 As indicated by the model simulation, sulfite oxidation in this system proceeds through an

363 efficient interfacial process alongside a slower bulk process. We propose that both the H_2O_2

364 oxidation pathway (R6-R10) and the $\text{SO}_3^{\bullet-}$ reaction mechanism (R11-R14) reported by Hung et

365 al.²⁷⁻²⁸ are plausible. Both processes may be enhanced at the interface. The key points discussed

366 here are summarized in Scheme 1 for the oxidation reaction at air-water interface.

367 The schematic shown proposes a gradient in ions and different species at the interface, i.e. the

368 stratification of ions as discussed by Litman et al.⁵² Sulfate ions have been shown to have a

369 propensity to move towards the aqueous bulk,⁵³ and sulfite may reside at the near-surface region

370 (but not at the interface).⁵³ A hydration layer at the interface may provide a buffer for direct surface

371 collisions.¹ These factors may explain the relatively low reactive uptake probabilities inferred in

372 this study.

373

374 4. Environmental Implications

375 While the interfacial reaction clearly leads to enhanced rates in the experimentally generated

376 particles ($<5 \mu\text{m}$ in radius in this study), we can further utilize our model to extrapolate these results

377 to the important and most atmospherically relevant size range for aqueous aerosols (including

378 submicron sizes). We find that the sulfate formation timescales in atmospherically relevant particles

379 are smaller than in larger particles, indicating that oxidation takes place more quickly, likely due to

the rate enhancement from an efficient interfacial reaction (Figure 5a). As compared to larger particles from laboratory experiments, formation timescales are ~1 order of magnitude smaller. The value of $1/\tau_{\text{sulfate}}$ for a particle of radius 0.24 μm , which is the average size in a typical sulfate distribution, is 0.108 min^{-1} .⁵⁴ This result indicates that efficient size-dependent chemistry is likely important in the atmosphere and could account for some of the missing sources of sulfate formation. Future implementation of the modeling framework developed here into atmospheric chemistry models will be necessary to test its relative significance.⁴⁰⁻⁴¹

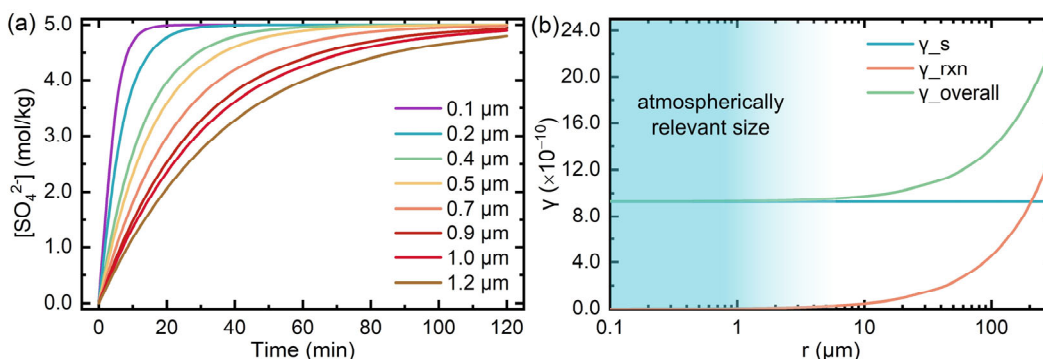


Figure 5. Simulated oxidation kinetics of sulfite oxidation within aqueous aerosols of atmospherically relevant size. (a) $[\text{S(VI)}]$ vs. time for aqueous aerosols with radii ranging from 0.1 – 1.2 μm . Near-complete oxidation is achieved across the size distribution within two hours. $T = 298 \text{ K}$, $\text{O}_2 = 21\%$. (b) Contributions of γ_s and γ_{rxn} to γ_{overall} at various sizes, with the atmospherically relevant region highlighted, plotted on a semi-log scale. The shaded region corresponds to the important size range of 0.1 to 1 μm .

Interestingly, the relative contributions of the bulk and surface processes (assuming the same kinetic parameters apply for an atmospherically relevant size range as to the larger microdroplets), show that the contribution of the surface reaction to the overall reactive uptake coefficient is significantly larger for smaller particles. As shown in the Figure 5b, the contribution of surface processes can account for nearly 100% when the aerosol radius is below 10 μm , then gradually decreased to ~50% when the aerosol radius is 200 μm . This is consistent with the observations of Li et al.³⁵, who noted the importance of the interfacial pathway for this system below the critical radius of 213 μm (Figure 5b).

Surface reactions for small particles are ~100 times faster than bulk-phase, and we show that the sulfate formation rate scales with increased temperatures and O_2 concentrations across the size distribution. This underscores the critical role of size-dependent chemistry in sulfate formation, potentially enhanced by the air-water interface of the aqueous aerosol. The interfacial electric field at the aqueous aerosol surface potentially initialized this enhanced surficial uncatalyzed oxidation. Overall, we show that size-dependent uncatalyzed sulfite oxidation is likely important in the atmosphere, and these insights will be used to improve model predictions of atmospheric sulfate formation.

AUTHOR INFORMATION

Corresponding Authors

Vicki H. Grassian – Department of Chemistry and Biochemistry, University of California San Diego, La Jolla, California 92093, USA. E-mail: vhgrassian@ucsd.edu

V. Faye McNeill – Department of Chemical Engineering, Columbia University, New York, New York 10027, USA. E-mail: vfm2103@columbia.edu

COMPETING INTERESTS DECLARATION

The authors declare no competing financial interest.

Author Contribution

VHG and VFM conceived the research. KG performed experiments and collected data. SS and VFM conducted the modeling. All authors participated in the writing of the manuscript.

ACKNOWLEDGMENTS

This work is supported by NSF AGS-2302301, AGS-2302302 and CHE-2203982.

SUPPORTING INFORMATION.

The contact angle of the super-hydrophobic substrate; S(IV) speciation diagram; Raman spectra of calibration bulk solutions and the calibration curves of sulfate and sulfite obtained from micro-Raman spectroscopy; Linear least-square fitting of the $\ln(C_{\text{sulfite}, t} / C_{\text{sulfite}, t=0})$ and reaction time within microdroplets; Optical images of several typical microdroplets.

REFERENCES

1. Ruiz-Lopez, M. F.; Francisco, J. S.; Martins-Costa, M. T. C.; Anglada, J. M., Molecular reactions at aqueous interfaces. *Nat. Rev. Chem.* **2020**, *4* (9), 459-475.
2. Yan, X.; Bain, R. M.; Cooks, R. G., Organic reactions in microdroplets: Reaction acceleration revealed by mass spectrometry. *Angew. Chem. Int. Ed. Engl.* **2016**, *55* (42), 12960-12972.
3. Liu, T.; Abbatt, J. P. D., Oxidation of sulfur dioxide by nitrogen dioxide accelerated at the interface of deliquesced aerosol particles. *Nat. Chem.* **2021**, *13* (12), 1173-1177.
4. Angle, K. J.; Neal, E. E.; Grassian, V. H., Enhanced rates of transition-metal-ion-catalyzed oxidation of S(IV) in aqueous aerosols: Insights into sulfate aerosol formation in the atmosphere. *Environ. Sci. Technol.* **2021**, *55* (15), 10291-10299.
5. Wang, W.; Liu, M.; Wang, T.; Song, Y.; Zhou, L.; Cao, J.; Hu, J.; Tang, G.; Chen, Z.; Li, Z.; Xu, Z.; Peng, C.; Lian, C.; Chen, Y.; Pan, Y.; Zhang, Y.; Sun, Y.; Li, W.; Zhu, T.; Tian, H.; Ge, M., Sulfate formation is dominated by manganese-catalyzed oxidation of SO₂ on aerosol surfaces during haze events. *Nat. Commun.* **2021**, *12* (1), 1993.
6. Li, M.; Boothby, C.; Continetti, R. E.; Grassian, V. H., Size-dependent sigmoidal reaction kinetics for pyruvic acid condensation at the air-water interface in aqueous microdroplets. *J. Am. Chem. Soc.* **2023**, *145* (41), 22317-22321.
7. Ge, Q.; Liu, Y.; Li, K.; Xie, L.; Ruan, X.; Wang, W.; Wang, L.; Wang, T.; You, W.; Zhang, L.,

454 Significant acceleration of photocatalytic CO₂ reduction at the gas-liquid interface of microdroplets.
 455 *Angew. Chem. Int. Ed. Engl.* **2023**, 62 (27), e202304189.

456 8. Lee, J. K.; Walker, K. L.; Han, H. S.; Kang, J.; Prinz, F. B.; Waymouth, R. M.; Nam, H. G.;
 457 Zare, R. N., Spontaneous generation of hydrogen peroxide from aqueous microdroplets. *Proc. Natl.*
 458 *Acad. Sci. U. S. A.* **2019**, 116 (39), 19294-19298.

459 9. Li, K.; Guo, Y.; Nizkorodov, S. A.; Rudich, Y.; Angelaki, M.; Wang, X.; An, T.; Perrier, S.;
 460 George, C., Spontaneous dark formation of OH radicals at the interface of aqueous atmospheric
 461 droplets. *Proc. Natl. Acad. Sci. U. S. A.* **2023**, 120 (15), e2220228120.

462 10. Holden, D. T.; Morato, N. M.; Cooks, R. G., Aqueous microdroplets enable abiotic synthesis
 463 and chain extension of unique peptide isomers from free amino acids. *Proc. Natl. Acad. Sci. U. S.*
 464 *A.* **2022**, 119 (42), e2212642119.

465 11. Li, K.; Gong, K.; Liu, J.; Ohnoute, L.; Ao, J.; Liu, Y.; Chen, X.; Xu, G.; Ruan, X.; Cheng, H.;
 466 Han, J.; Sui, G.; Ji, M.; Valev, V. K.; Zhang, L., Significantly accelerated photochemical and
 467 photocatalytic reactions in microdroplets. *Cell Rep. Phys. Sci.* **2022**, 3 (6).

468 12. Gong, K.; Ao, J.; Li, K.; Liu, L.; Liu, Y.; Xu, G.; Wang, T.; Cheng, H.; Wang, Z.; Zhang, X.;
 469 Wei, H.; George, C.; Mellouki, A.; Herrmann, H.; Wang, L.; Chen, J.; Ji, M.; Zhang, L.; Francisco,
 470 J. S., Imaging of pH distribution inside individual microdroplet by stimulated Raman microscopy.
 471 *Proc. Natl. Acad. Sci. U. S. A.* **2023**, 120 (20), e2219588120.

472 13. Qiu, L.; Wei, Z.; Nie, H.; Cooks, R. G., Reaction acceleration promoted by partial solvation at
 473 the gas/solution interface. *Chempluschem* **2021**, 86 (10), 1362-1365.

474 14. Xiong, H.; Lee, J. K.; Zare, R. N.; Min, W., Strong concentration enhancement of molecules
 475 at the interface of aqueous microdroplets. *J. Phys. Chem. B* **2020**, 124 (44), 9938-9944.

476 15. Martins-Costa, M. T. C.; Ruiz-Lopez, M. F., Electrostatics and chemical reactivity at the air-
 477 water interface. *J. Am. Chem. Soc.* **2023**, 145 (2), 1400-1406.

478 16. Hao, H.; Leven, I.; Head-Gordon, T., Can electric fields drive chemistry for an aqueous
 479 microdroplet? *Nat. Commun.* **2022**, 13 (1), 280.

480 17. Xiong, H.; Lee, J. K.; Zare, R. N.; Min, W., Strong electric field observed at the interface of
 481 aqueous microdroplets. *J. Phys. Chem. Lett.* **2020**, 11 (17), 7423-7428.

482 18. Zhu, C.; Pham, L. N.; Yuan, X.; Ouyang, H.; Coote, M. L.; Zhang, X., High electric fields on
 483 water microdroplets catalyze spontaneous and fast reactions in halogen-bond complexes. *J. Am.*
 484 *Chem. Soc.* **2023**, 145 (39), 21207-21212.

485 19. Lee, J. K.; Samanta, D.; Nam, H. G.; Zare, R. N., Micrometer-sized water droplets induce
 486 spontaneous reduction. *J. Am. Chem. Soc.* **2019**, 141 (27), 10585-10589.

487 20. Qiu, L.; Psimos, M. D.; Cooks, R. G., Spontaneous oxidation of aromatic sulfones to sulfonic
 488 acids in microdroplets. *J. Am. Soc. Mass. Spectrom.* **2022**, 33 (8), 1362-1367.

489 21. Xing, D.; Yuan, X.; Liang, C.; Jin, T.; Zhang, S.; Zhang, X., Spontaneous oxidation of I⁻ in
 490 water microdroplets and its atmospheric implications. *Chem. Commun.* **2022**, 58 (89), 12447-12450.

491 22. Mehrgardi, M. A.; Mofidfar, M.; Zare, R. N., Sprayed water microdroplets are able to generate
 492 hydrogen peroxide spontaneously. *J. Am. Chem. Soc.* **2022**, 144 (17), 7606-7609.

493 23. Colussi, A. J., Mechanism of hydrogen peroxide formation on sprayed water microdroplets. *J.*
 494 *Am. Chem. Soc.* **2023**, 145 (30), 16315-16317.

- 495 24. Zheng, B.; Zhang, Q.; Zhang, Y.; He, K. B.; Wang, K.; Zheng, G. J.; Duan, F. K.; Ma, Y. L.;
 496 Kimoto, T., Heterogeneous chemistry: a mechanism missing in current models to explain secondary
 497 inorganic aerosol formation during the January 2013 haze episode in North China. *Atmos. Chem.*
 498 *Phys.* **2015**, *15* (4), 2031-2049.
- 499 25. Cheng, Y. F.; Zheng, G. J.; Wei, C.; Mu, Q.; Zheng, B.; Wang, Z. B.; Gao, M.; Zhang, Q.; He,
 500 K. B.; Carmichael, G.; Poschl, U.; Su, H., Reactive nitrogen chemistry in aerosol water as a source
 501 of sulfate during haze events in China. *Sci. Adv.* **2016**, *2* (12).
- 502 26. Chen, Z.; Liu, P.; Wang, W.; Cao, X.; Liu, Y. X.; Zhang, Y. H.; Ge, M., Rapid sulfate formation
 503 via uncatalyzed autoxidation of sulfur dioxide in aerosol microdroplets. *Environ. Sci. Technol.* **2022**,
 504 *56* (12), 7637-7646.
- 505 27. Hung, H. M.; Hoffmann, M. R., Oxidation of gas-phase SO₂ on the surfaces of acidic
 506 microdroplets: Implications for sulfate and sulfate radical anion formation in the atmospheric liquid
 507 phase. *Environ. Sci. Technol.* **2015**, *49* (23), 13768-76.
- 508 28. Hung, H. M.; Hsu, M. N.; Hoffmann, M. R., Quantification of SO₂ oxidation on interfacial
 509 surfaces of acidic micro-droplets: Implication for ambient sulfate formation. *Environ. Sci. Technol.*
 510 **2018**, *52* (16), 9079-9086.
- 511 29. Liu, Y.; Ge, Q.; Wang, T.; Zhang, R.; Li, K.; Gong, K.; Xie, L.; Wang, W.; Wang, L.; You, W.;
 512 Ruan, X.; Shi, Z.; Han, J.; Wang, R.; Fu, H.; Chen, J.; Chan, C. K.; Zhang, L., Strong electric field
 513 force at the air/water interface drives fast sulfate production in the atmosphere. *Chem* **2024**, *10* (1),
 514 330-351.
- 515 30. Wang, W.; Liu, Y.; Wang, T.; Ge, Q.; Li, K.; Liu, J.; You, W.; Wang, L.; Xie, L.; Fu, H.; Chen,
 516 J.; Zhang, L., Significantly accelerated photosensitized formation of atmospheric sulfate at the air-
 517 water interface of microdroplets. *J. Am. Chem. Soc.* **2024**, *146* (10), 6580-6590.
- 518 31. Jing, X.; Chen, Z.; Cao, X.; Huang, Q.; Liu, P.; Zhang, Y.-h., Rapid sulfate formation via Mn²⁺-
 519 catalyzed SO₂ oxidation on the surface of NaCl microdroplets. *J. Phys. Chem. C* **2023**, *127* (28),
 520 13632-13638.
- 521 32. Tarbuck, T. L.; Richmond, G. L., SO₂:H₂O surface complex found at the vapor/water interface.
 522 *J. Am. Chem. Soc.* **2005**, *127* (48), 16806-7.
- 523 33. Zhong, J.; Zhu, C.; Li, L.; Richmond, G. L.; Francisco, J. S.; Zeng, X. C., Interaction of SO₂
 524 with the surface of a water nanodroplet. *J. Am. Chem. Soc.* **2017**, *139* (47), 17168-17174.
- 525 34. Cao, X.; Liu, Y. X.; Huang, Q.; Chen, Z.; Sun, J.; Sun, J.; Pang, S. F.; Liu, P.; Wang, W.; Zhang,
 526 Y. H.; Ge, M., Single droplet tweezer revealing the reaction mechanism of Mn(II)-catalyzed SO₂
 527 oxidation. *Environ. Sci. Technol.* **2024**, *58* (11), 5068-5078.
- 528 35. Li, L.-F.; Liu, P.; Huang, Q.; Zhang, X.; Chao, X.; Pang, S.; Wang, W.; Cheng, Y.; Su, H.;
 529 Zhang, Y.-H.; Ge, M., Rethinking urban haze formation: Atmospheric sulfite conversion rate scales
 530 with aerosol surface area, not volume. *One Earth* **2024**, *7* (6), 1082-1095.
- 531 36. Yang, J.; Li, L.; Wang, S.; Li, H.; Francisco, J. S.; Zeng, X. C.; Gao, Y., Unraveling a new
 532 chemical mechanism of missing sulfate formation in aerosol haze: Gaseous NO₂ with aqueous
 533 HSO₃⁻/SO₃²⁻. *J. Am. Chem. Soc.* **2019**, *141* (49), 19312-19320.
- 534 37. Chen, X.; Xia, Y.; Zhang, Z.; Hua, L.; Jia, X.; Wang, F.; Zare, R. N., Hydrocarbon degradation
 535 by contact with anoxic water microdroplets. *J. Am. Chem. Soc.* **2023**, *145* (39), 21538-21545.

38. Liu, T.; Chan, A. W. H.; Abbatt, J. P. D., Multiphase oxidation of sulfur dioxide in aerosol particles: Implications for sulfate formation in polluted environments. *Environ. Sci. Technol.* **2021**, *55* (8), 4227-4242.
39. Radojević, M., On the discrepancy between reported studies of the uncatalysed aqueous oxidation of SO₂ by O₂. *Environ. Technol.* **2008**, *5* (12), 549-566.
40. Tsui, W. G.; Rao, Y.; Dai, H. L.; McNeill, V. F., Modeling photosensitized secondary organic aerosol formation in laboratory and ambient aerosols. *Environ. Sci. Technol.* **2017**, *51* (13), 7496-7501.
41. Tsui, W. G.; McNeill, V. F., Modeling secondary organic aerosol production from photosensitized humic-like substances (HULIS). *Environ. Sci. Tech. Lett.* **2018**, *5* (5), 255-259.
42. Wei, H.; Vejerano, E. P.; Leng, W.; Huang, Q.; Willner, M. R.; Marr, L. C.; Vikesland, P. J., Aerosol microdroplets exhibit a stable pH gradient. *Proc. Natl. Acad. Sci. U. S. A.* **2018**, *115* (28), 7272-7277.
43. Shao, J.; Chen, Q.; Wang, Y.; Lu, X.; He, P.; Sun, Y.; Shah, V.; Martin, R. V.; Philip, S.; Song, S.; Zhao, Y.; Xie, Z.; Zhang, L.; Alexander, B., Heterogeneous sulfate aerosol formation mechanisms during wintertime Chinese haze events: air quality model assessment using observations of sulfate oxygen isotopes in Beijing. *Atmos. Chem. Phys.* **2019**, *19* (9), 6107-6123.
44. Chung, K. Y.; Yoon, W.-S.; McBreen, J.; Yang, X.-Q.; Oh, S. H.; Shin, H. C.; Cho, W. I.; Cho, B. W., In situ X-ray diffraction studies on the mechanism of capacity retention improvement by coating at the surface of LiCoO₂. *J. Power Sources* **2007**, *174* (2), 619-623.
45. Worsnop, D. R.; Morris, J. W.; Shi, Q.; Davidovits, P.; Kolb, C. E., A chemical kinetic model for reactive transformations of aerosol particles. *Geophys. Res. Lett.* **2002**, *29* (20).
46. Coddens, E. M.; Angle, K. J.; Grassian, V. H., Titration of aerosol pH through droplet coalescence. *J. Phys. Chem. Lett.* **2019**, *10* (15), 4476-4483.
47. Bishop, C. M.; Nasrabadi, N. M., *Pattern recognition and machine learning*. Springer: 2006; Vol. 4.
48. Tomobe, K.; Yamamoto, E.; Kojic, D.; Sato, Y.; Yasui, M.; Yasuoka, K., Origin of the blueshift of water molecules at interfaces of hydrophilic cyclic compounds. *Sci. Adv.* **2017**, *3* (12), e1701400.
49. Angelaki, M.; d'Erceville, J.; Donaldson, D. J.; George, C., pH Affects the spontaneous formation of H₂O₂ at the air-water interfaces. *J. Am. Chem. Soc.* **2024**, *146* (38), 25889-25893.
50. de la Puente, M.; Laage, D., How the acidity of water droplets and films is controlled by the air-water interface. *J. Am. Chem. Soc.* **2023**, *145* (46), 25186-25194.
51. Tse, Y. L.; Chen, C.; Lindberg, G. E.; Kumar, R.; Voth, G. A., Propensity of hydrated excess protons and hydroxide anions for the air-water interface. *J. Am. Chem. Soc.* **2015**, *137* (39), 12610-6.
52. Litman, Y.; Chiang, K. Y.; Seki, T.; Nagata, Y.; Bonn, M., Surface stratification determines the interfacial water structure of simple electrolyte solutions. *Nat. Chem.* **2024**, *16* (4), 644-650.
53. Jungwirth, P.; Curtis, J. E.; Tobias, D. J., Polarizability and aqueous solvation of the sulfate dianion. *Chem. Phys. Lett.* **2003**, *367* (5-6), 704-710.
54. Whitby, K. T., The physical characteristics of sulfur aerosols. *Atmos. Environ.* **1978**, *12* (1-3), 135-159.

Supporting information for

Size Dependent Uncatalyzed Sulfite Oxidation in Aqueous Microdroplets

Kedong Gong,¹ Sandhya Sethuraman,² Zifeng Tang,² V. Faye McNeill^{2,3*} and Vicki H. Grassian^{1*}

¹Department of Chemistry and Biochemistry, University of California San Diego, La Jolla,
CA 92093, United States

²Department of Chemical Engineering, Columbia University
New York, NY 10027, United States

²Department of Earth and Environmental Sciences, Columbia University
New York, NY 10027, United States

*Corresponding Authors. Email: vhgrassian@ucsd.edu (V.H.G) and vfm2103@columbia.edu
(V.F.M.)

This file includes figures S1 to S16, Table S1, and two references

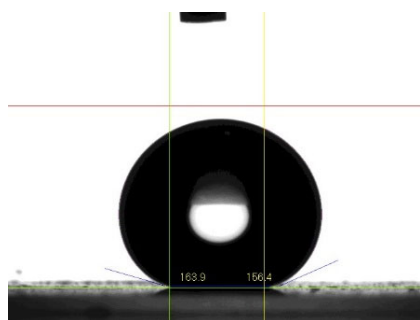


Figure S1. The contact angle of the super-hydrophobic substrate. The average of the measured contact angle between the aqueous microdroplet and the superhydrophobic quartz substrate is $160.1 \pm 3.35^\circ$.

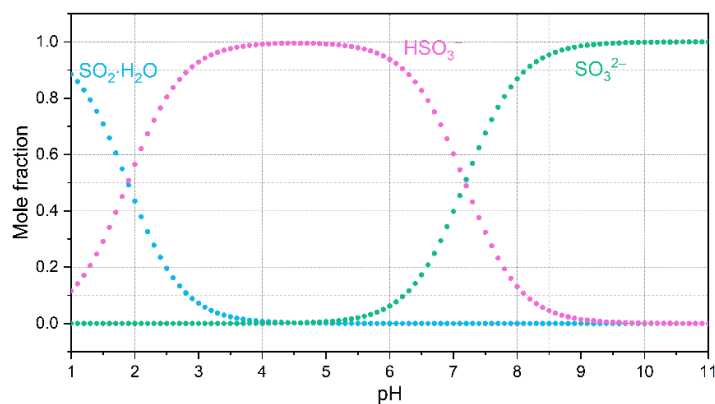


Figure S2. S(IV) speciation diagram. The distribution of different S(IV) species is shown as a function of bulk solution pH.¹

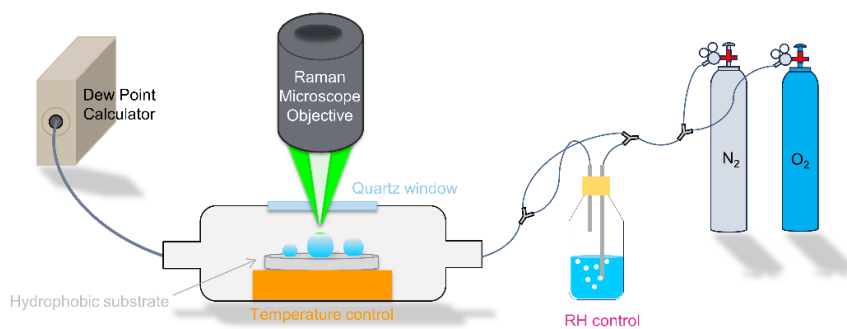


Figure S3. Schematic of the experimental setup for *in-situ* microdroplet detection with confocal Raman spectroscopy.

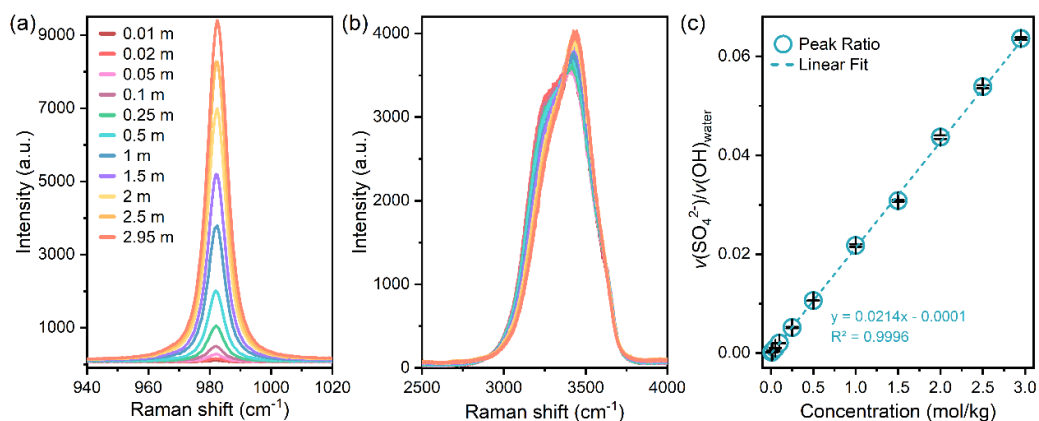


Figure S4. Calibration curve of sulfate concentration with micro-Raman spectroscopy. The solution phase spectra of the sulfate and water peaks are shown along with the resulting sulfate calibration curve. Raman spectrum of (a) $\nu_s(\text{SO}_4^{2-})$ at 980 cm^{-1} and (b) $\nu(\text{OH})_{\text{water}}$ at 3420 cm^{-1} from standard Na_2SO_4 bulk solutions. (c) The calibration curve relating $[\text{SO}_4^{2-}]$ to the peak area ratio of $\nu_s(\text{SO}_4^{2-})/\nu(\text{OH})_{\text{water}}$.

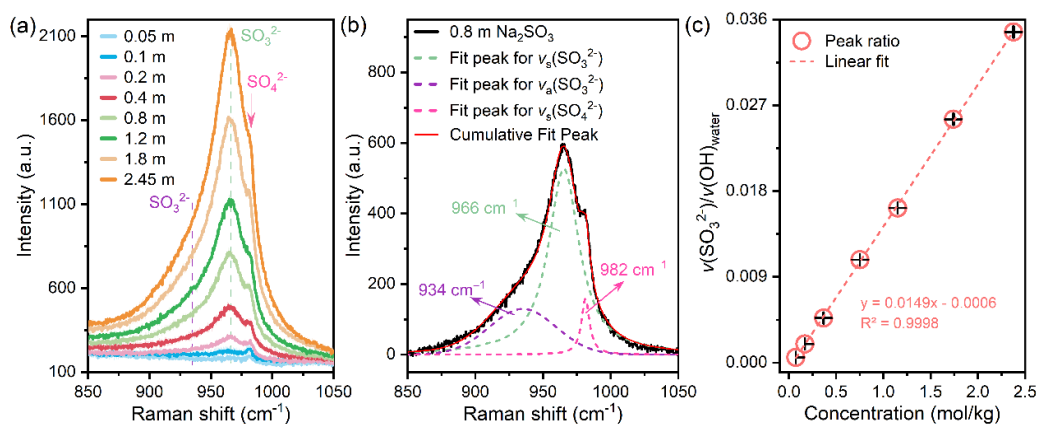


Figure S5. Calibration curve of sulfite concentration with micro-Raman spectroscopy. The solution phase spectra and the resulting calibration curve to determine sulfite concentrations in microdroplets are shown. (a) Raman spectra of the $\nu_s(\text{SO}_3^{2-})$ at 934 cm^{-1} , $\nu_a(\text{SO}_3^{2-})$ at 966 cm^{-1} , and $\nu_s(\text{SO}_4^{2-})$ at 980 cm^{-1} from standard Na_2SO_3 bulk solutions.² (b) Peak curve fitting and analysis of a representative Raman spectrum for a 0.8 mol/kg Na_2SO_3 solution. (c) Calibration curve relating $[\text{SO}_3^{2-}]$ to the peak area ratio of $\nu_s(\text{SO}_3^{2-})/\nu(\text{OH})_{\text{water}}$.

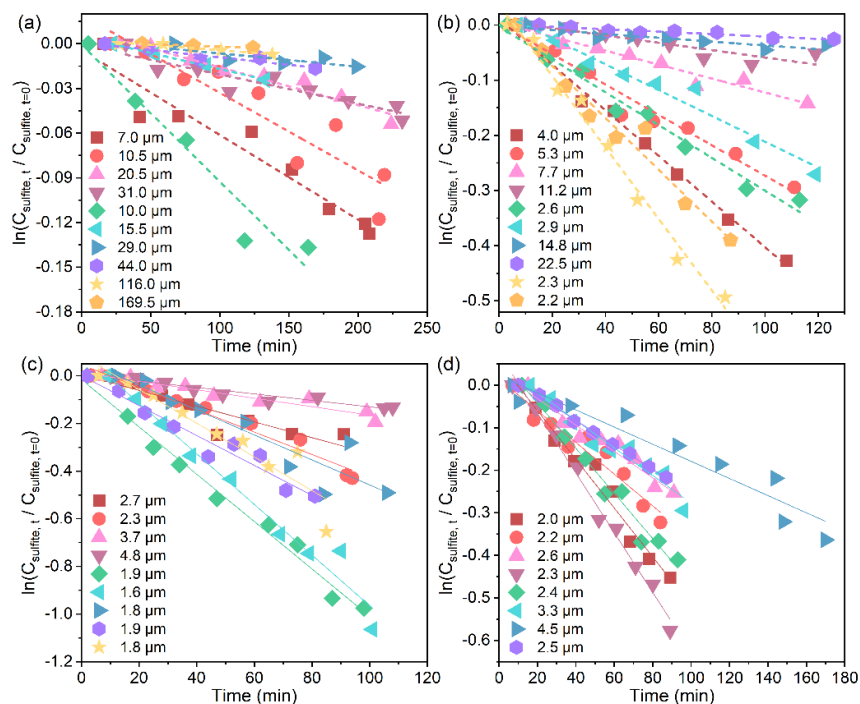


Figure S6. Linear least-square fitting of the $\ln(C_{\text{sulfite},t} / C_{\text{sulfite},t=0})$ and reaction time. Uncatalyzed sulfite oxidation by 9% O_2 at $T = 298 \text{ K}$ in substrate deposited microdroplets of different sizes.

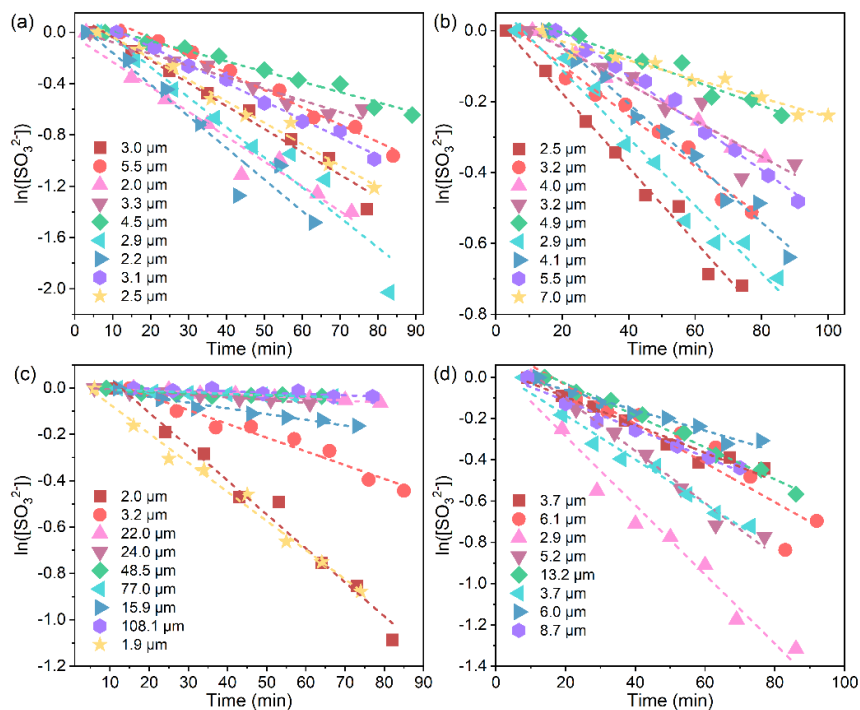


Figure S7. Linear least-square fitting of the $\ln(C_{\text{sulfite},t} / C_{\text{sulfite},t=0})$ and reaction time. Uncatalyzed sulfite oxidation by 21% O_2 at $T = 298 \text{ K}$ in substrate deposited microdroplets of different sizes.

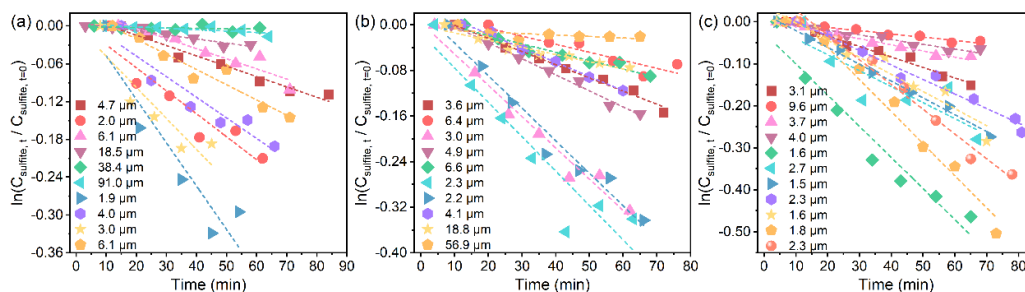


Figure S8. Linear least-square fitting of the $\ln(C_{\text{sulfite},t} / C_{\text{sulfite},t=0})$ and reaction time. Uncatalyzed sulfite oxidation by 21% O_2 at $T = 278 \text{ K}$ in substrate deposited microdroplets of different sizes.

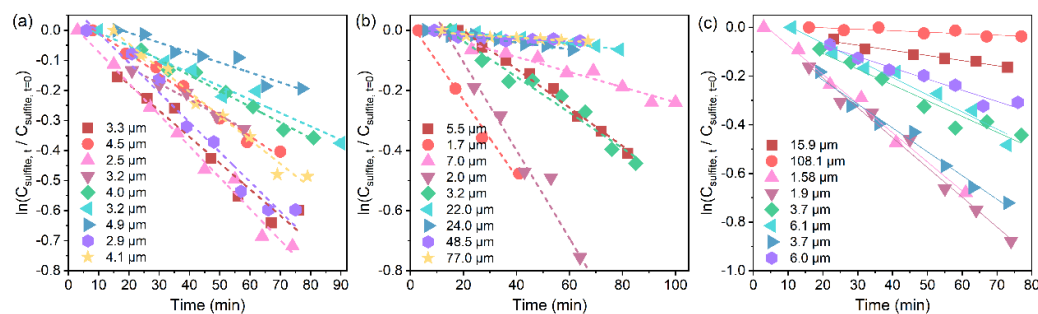


Figure S9. Linear least-square fitting of the $\ln(C_{\text{sulfite},t} / C_{\text{sulfite},t=0})$ and reaction time. Uncatalyzed sulfite oxidation by 21% O_2 at $T = 288 \text{ K}$ in substrate deposited microdroplets of different sizes.

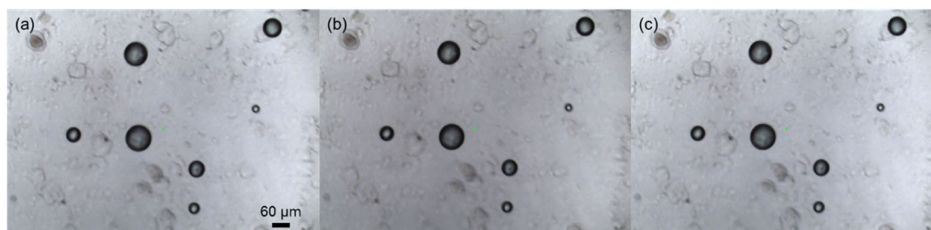


Figure S10. Microdroplet size during sulfite oxidation. The microdroplet size remains constant during sulfite oxidation. Optical images of several microdroplets are shown at reaction times of (a) 0 min, (b) 60 min, and (c) 120 min under the reaction conditions of 21% O_2 , a temperature of 298 K, and a relative humidity of 80%.

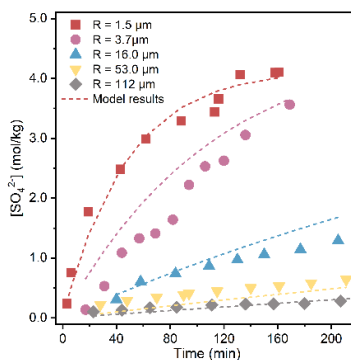


Figure S11. Time evolution of the SO_4^{2-} concentration ($[\text{SO}_4^{2-}]$) for aqueous microdroplets of varying radius and a bulk solution with the corresponding model simulation results.

Table S1. R² and RMSE values for the model fits on experimental data across all four experiments.

Experiment	R2	RMSE	Normalized RMSE
298 K, 21% O2	0.922	0.002	0.248
298 K, 9% O2	0.755	0.001	0.457
288 K, 21% O2	0.811	0.002	0.284
278K, 21% O2	0.604	0.001	0.441

References

1. Seinfeld, J. H.; Pandis, S. N., *Atmospheric chemistry and physics: from air pollution to climate change*. John Wiley & Sons: 2016.
2. Risberg, E. D.; Eriksson, L.; Mink, J.; Pettersson, L. G.; Skripkin, M. Y.; Sandstrom, M., Sulfur X-ray absorption and vibrational spectroscopic study of sulfur dioxide, sulfite, and sulfonate solutions and of the substituted sulfonate ions X3CSO3⁻ (X = H, Cl, F). *Inorg Chem* **2007**, *46* (20), 8332-48.